nature materials

ARTICLES

https://doi.org/10.1038/s41563-022-01249-7

Porosity-based heterojunctions enable leadless optoelectronic modulation of tissues

Aleksander Prominski[1,2,3], Jiuyun Shi[1,2,3], Pengju Li[4], Jiping Yue[1], Yiliang Lin[1,2,3], Jihun Park[1,2,3], Bozhi Tian[1,2,3]✉ and Menahem Y. Rotenberg[5]✉

Homo- and heterojunctions play essential roles in semiconductor-based devices such as field-effect transistors, solar cells, photodetectors and light-emitting diodes. Semiconductor junctions have been recently used to optically trigger biological modulation via photovoltaic or photoelectrochemical mechanisms. The creation of heterojunctions typically involves materials with different doping or composition, which leads to high cost, complex fabrications and potential side effects at biointerfaces. Here we show that a porosity-based heterojunction, a largely overlooked system in materials science, can yield an efficient photoelectrochemical response from the semiconductor surface. Using self-limiting stain etching, we create a nanoporous/non-porous, soft–hard heterojunction in p-type silicon within seconds under ambient conditions. Upon surface oxidation, the heterojunction yields a strong photoelectrochemical response in saline. Without any interconnects or metal modifications, the heterojunction enables efficient non-genetic optoelectronic stimulation of isolated rat hearts ex vivo and sciatic nerves in vivo with optical power comparable to optogenetics, and with near-infrared capabilities.

Flexible bioelectronic devices are extensively employed in bioengineering applications, including drug delivery[1], physiology sensing[1–4] and bioelectrical modulation[1–3,5]. Advances in this area have almost eliminated the challenge of biomechanical mismatch[6]; however, the leads of most flexible bioelectronic devices are still associated with potential complications, such as infection[7–9], thrombosis[8,10] and anatomical position limitations[11,12]. Thus, extensive effort has been invested in the development of leadless biomodulation techniques. Pulsed infrared lasers have been utilized to induce a photothermal effect, which allows neuronal[13,14] and cardiac[15,16] tissue modulation; however, the required high power densities and the infrared laser absorbance by water hinders therapeutic implementation. As an alternative, optogenetics has been successfully employed for neuromodulation[17,18] and cardiac pacing[19] in vivo, but the need for genetic manipulation would limit its clinical translation. Leadless bioresorbable devices used magnetic induction to perform neural regenerative medicine[20] and cardiac pacing[21], while ultrasonic transducers enabled leadless neuromodulation[22]. Another approach to leadless modulation involves the application of semiconductor materials that can harvest and convert light into an electrical or optoelectronic stimulus[23–25]. Most of these designs rely on a photodiode configuration in which either p–n or p–i–n junctions are created by doping variation in successive layers. Furthermore, to generate sufficient photocurrents, the surface of the silicon p–i–n junction must be decorated with metals and necessitates high power densities of light[5], which limits their therapeutic utility.

An alternative, yet much less explored, strategy for diode-like performance involves creating a nanoporous/non-porous semiconductor heterojunction[26–28], wherein the nanoporous and non-porous semiconductor components display different band structures (Fig. 1a). Such a porosity-based semiconductor heterojunction has not been used for bioelectronics studies, to the best of our knowledge. However, it represents an appealing candidate as it yields a pure semiconductor–biofluids interface (free of dopant modulation or metal decoration) and a potentially more deformable biointerface due to the porosity of the interfacing nanoporous layer[29,30].

In this work, we develop a fast and efficient method for obtaining pure-silicon porosity-based heterojunctions with strong photoelectrochemical properties by combining stain etching and a high-power oxygen plasma treatment. This method allows a simple and straightforward fabrication of optoelectronic devices out of bulk silicon, a process that thus far had required extensive and sophisticated instrumentation, as in bottom-up (for example, chemical vapour deposition) or top-down fabrication approaches. To demonstrate the utility of such materials in optically induced biomodulation, we fabricated flexible crystalline silicon membranes that transduce light pulses with low optical power densities to allow overdrive heart pacing and nerve bundle activation leading to skeletal muscle contraction (Fig. 1b). Besides the lack of genetic modification, another advantage over optogenetics is the ability of these devices to modulate the tissues with tissue-penetrating near-infrared (NIR) light, suggesting their potential in diverse therapeutic applications.

Synthesis and structure of nanoporous heterojunctions

Stain etching is a type of electroless etching enabled by hole injection from strong oxidants in solution phase into the valence band of semiconductors[31]. Stain etching can produce different types of porous structures on the surface of silicon, and this porous silicon has been explored as coating layers in photovoltaics, photoluminescent agents in bioimaging and active electrode components in lithium batteries. Porous silicon has an enlarged bandgap compared with bulk silicon[26]; however, the photoelectrochemical performance of a nanoporous/non-porous silicon heterojunction has not been leveraged for any bioelectronics applications, to the best of our

[1]Department of Chemistry, The University of Chicago, Chicago, IL, USA. [2]The James Franck Institute, The University of Chicago, Chicago, IL, USA. [3]The Institute for Biophysical Dynamics, The University of Chicago, Chicago, IL, USA. [4]The Pritzker School of Molecular Engineering, The University of Chicago, Chicago, IL, USA. [5]Department of Biomedical Engineering, Technion – Israel Institute of Technology, Haifa, Israel. ✉e-mail: btian@uchicago.edu; hemir@bm.technion.ac.il

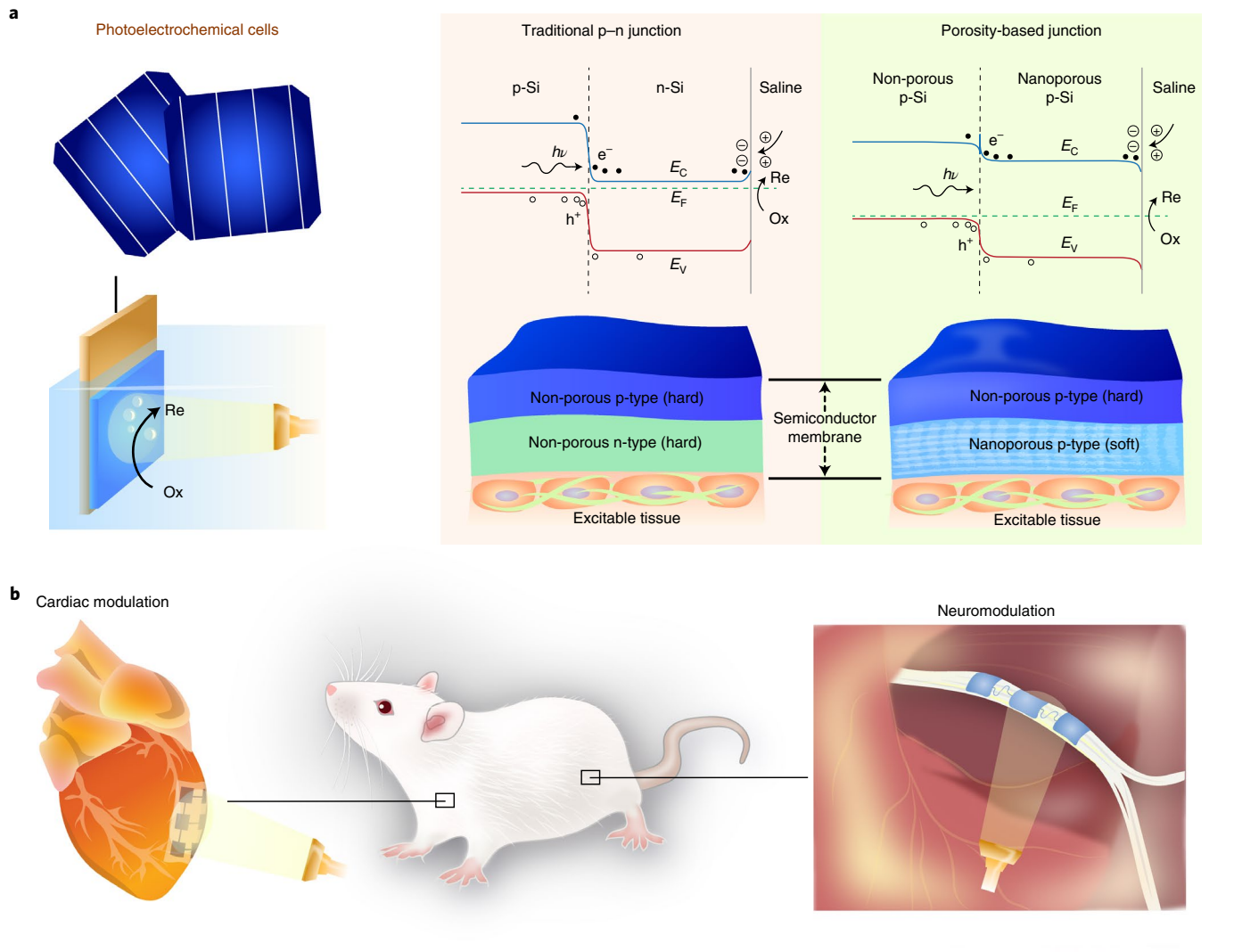

Fig. 1 | Nanoporous/non-porous silicon materials enable efficient photoelectrochemical effects, and their biomimetic structure makes them suitable for application in biointerfaces. a, Diodes are the key building blocks for solar cells and photoelectrochemical cells. The p–n junction creates a built-in electrical field that separates the light-generated electrons (e^-) and holes (h^+). In a photocathodic reaction, the electrons can reach the surface of an n-type silicon for reduction reactions. A difference in porosity can create a diode-like band alignment in a p-type silicon. This heterojunction demonstrates strong photoelectrochemical properties without the need for dopant modulation. Moreover, the porous surface yields a softer biointerface, which may further reduce the biomechanical mismatch. Re, reductant; Ox, oxidant; E_V, valence band edge; E_C, conduction band edge; E_F, Fermi level; $h\nu$, photon energy. **b**, Thin and flexible nanoporous/non-porous silicon membranes allow stimulation of rat hearts ex vivo and sciatic nerves in vivo using low-energy light pulses.

knowledge. Instead, the focus of silicon nanostructuring has been aimed at improving light absorbance and reducing surface impedance[32]. Moreover, the field has been engulfed by efforts focused on metal-assisted chemical etching, which have produced many nanostructures from photolithography-defined metal masks[33]. However, while metal-assisted etching can be used to obtain a variety of morphologies, the semiconductor–metal junctions introduce additional complexity to the system. Thus, the benefits of metal-free self-limiting etching fabrications should not be overlooked, as the simplicity of the process and purity of the material can lead to improved biocompatibility and stability.

We used metal-free etching with hydrofluoric acid and nitric acid to generate nanoporous/non-porous silicon heterojunctions directly in p-type crystalline silicon. Scanning electron microscopy showed the formation of porous structures and micro-sized pillars on the surface of the silicon (Fig. 2a). The sponge-like pore morphology was independent of etching time (Supplementary Fig. 1), but the pillars tended to grow and coalesce over time (Supplementary Fig. 2). Pillar height was determined by atomic force microscopy to be in the range of hundreds of nanometres (Fig. 2b). We attribute the formation of micropillars to the coalescence of hydrogen bubbles (self-masking process), which results in hierarchical surface morphology (Fig. 2c). Cross-sectional microscopy showed that while the thickness of the nanoporous layer correlated poorly with etching time, the microstructured pillars grew continuously during etching (Supplementary Fig. 3). The micropillars formed during etching may contribute to enhanced photoelectrochemical properties through increased surface light trapping[32].

We used scanning transmission electron microscopy (STEM) to further understand the microscopic structure of the material. STEM images showed a sharp interface between nanoporous and non-porous domains in a pure silicon sample (Fig. 2d). Selected area electron diffraction patterns revealed that both domains and their interface were a coherent single crystal. High-magnification

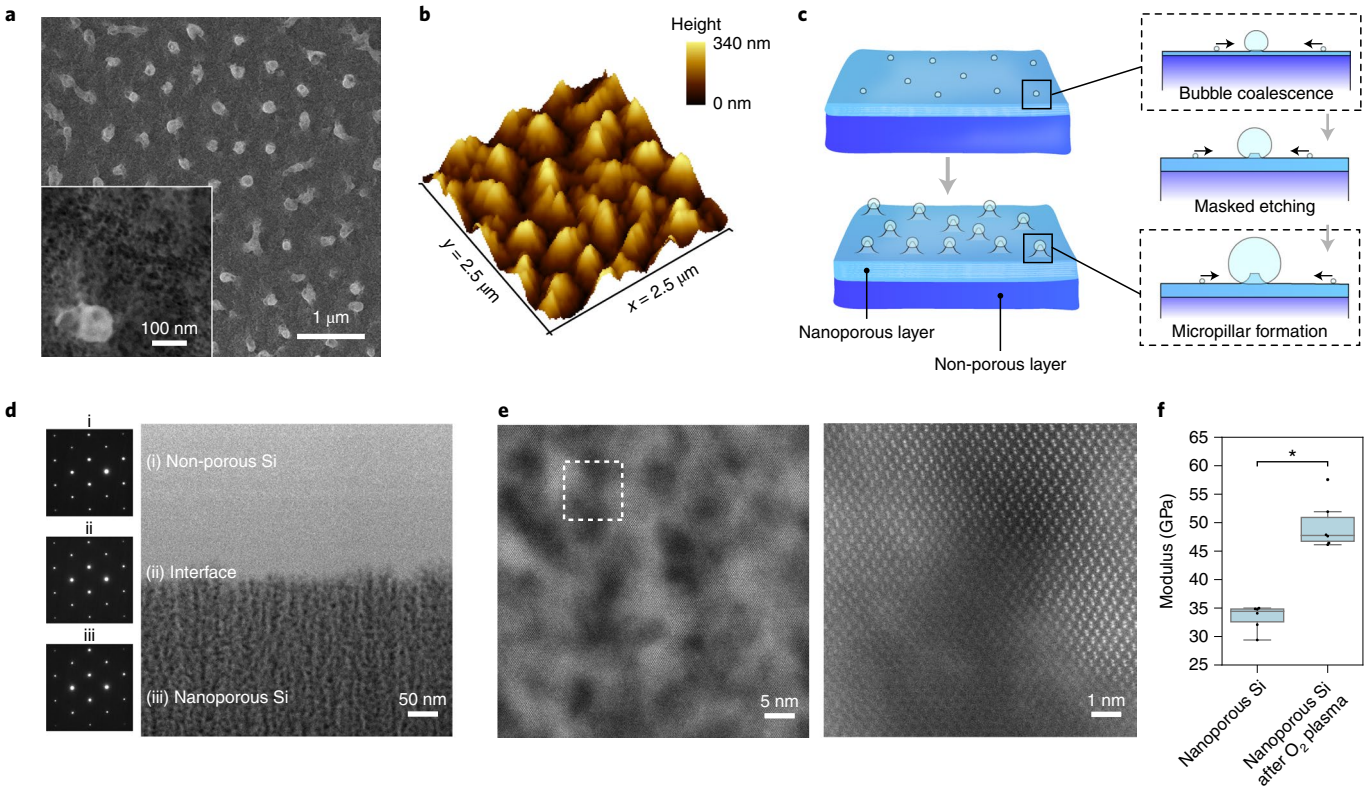

Fig. 2 | Microscopy analysis of the material structure. a, A scanning electron microscopy image shows porosification of the material surface and formation of microscale pillars. The inset shows a porous surface. **b**, Three-dimensional reconstruction of the material surface from an atomic force microscopy scan shows that the height of the pillar-like structures is hundreds of nanometres. Results are representative of over three independent experiments. **c**, Formation of micropillars can be attributed to the coalescence of hydrogen bubbles during wet etching. Schematic presents the proposed model of self-masking leading to pillar formation. **d**, An STEM image shows the interface between the non-porous and nanoporous silicon in the material. Selected area electron diffraction patterns taken on different material domains and along [110] zone axis show the same crystalline diffraction pattern and no signs of amorphization. **e**, High-magnification STEM images show crystallinity in the nanoporous region. Characterization was performed on samples etched for 1 min in 1% HNO_3 in HF (v/v). A single focused ion beam section of the material was prepared and imaged with STEM in this study. The image on the right shows the area in the dashed box on the left. **f**, Elastic modulus of nanoporous silicon samples. Three measurements on two samples were performed for a number of measurements, $N_{meas} = 6$. Boxes bind the interquartile range (IQR) divided by the median; whiskers extend 1.5 ± IQR. All datapoints are plotted. Statistics are calculated using Student's *t*-test, two-sided. *P* values for comparisons are shown: $^*P < 0.001$.

STEM images (Fig. 2e) further confirmed the crystalline lattice of the nanoporous silicon domain. A coherent single-crystal structure yields efficient charge transport due to the absence of amorphous regimes, while the nano-sized features in the nanoporous domain produce the band shift necessary to enable diode-like behaviour (Fig. 1a) through the quantum confinement effect.

Next, we used indentation to study the mechanical properties of the nanoporous layer. We determined the elastic modulus of the nanoporous silicon layer to be 33 ± 2 GPa (Fig. 2f and Supplementary Fig. 4), which is smaller than that of single-crystalline silicon[34]. An oxygen plasma treatment increased the modulus to 50 ± 4 GPa (Fig. 2f), which suggests that oxidation of the nanoporous silicon may mitigate the mechanical impact of the structural defects in silicon by introducing the atomic-scale or nanoscale oxide phase. Additionally, we used spectroscopic ellipsometry to determine the uniformity of the porous layer. The high homogeneity of elliptical properties can be found locally on a surface area of submillimetre scale. However, when areas of over 1 mm were scanned, larger differences were observed, probably due to changes in the material roughness (Supplementary Fig. 5). However, such differences do not seem to affect the photoelectrochemical properties of the material, which were found to be uniform, as described in the following sections.

Enhancement in photocurrent generation

To create a highly efficient photoelectrochemical silicon surface, we investigated different stain etching conditions with oxygen plasma treatment. We used our previously reported patch-clamp photoresponse measurement set-up (Fig. 3a) to screen a large set of etching conditions on bulk silicon wafers and silicon membranes[35]. In our analysis, we focused on the total charge injection over the illumination period, and the contributions coming from capacitive and faradaic currents (Fig. 3b) determined from the numerical analysis of recorded current transients. For each etching condition, we performed measurements before and after oxygen plasma treatment. Figure 3c shows photocurrents achieved using 1% (v/v) nitric acid in concentrated (50%) hydrofluoric acid. We have found that the majority of the injected charge originates from the capacitive effect, and faradaic currents account for only 4% of the total charge, and less if shorter light pulses are used. Oxygen plasma treatment enhanced the photocurrents for etching times between 1 and 20 min, with comparable saturation levels. The time independence of the achieved photocurrents may be due to the self-limiting nature of the stain etching process; the valence band of the porous silicon becomessufficiently low such that hole injection and over-etching are inhibited. We found that even 10 s of stain etching was sufficient to transform non-photoresponsive p-type silicon wafers into strong photoresponsive materials (Fig. 3d).

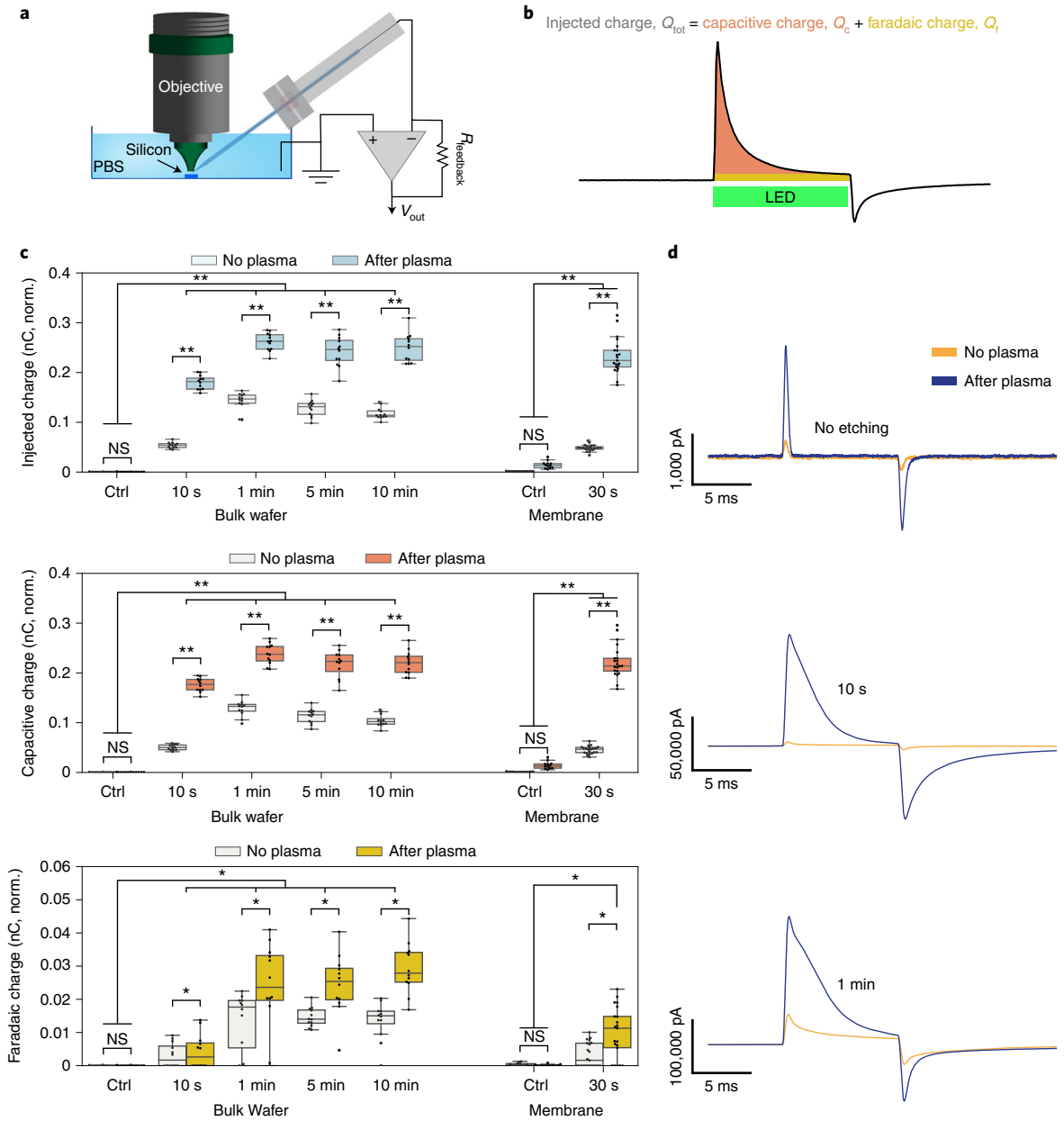

Fig. 3 | Screening of etching conditions for photocurrent generation. a, Schematic of the patch-clamp integrated photocurrent measurement set-up used to study wafers and membranes. $R_{feedback}$, resistance of a feedback resistor for the amplifier; V_{out}, amplifier output voltage. **b**, Schematic of the photocurrent transient (black line) with definition of the total injected charge (Q_{tot}), capacitive charge (Q_c) and faradaic charge (Q_f) used as figures of merit in the optimization of the material processing parameters. LED, light-emitting diode. **c**, Photocurrents measured from p-type silicon materials under different etching times with 1% nitric acid. Even short etching times (10 s) are sufficient to generate strong photocurrents from the materials. Oxygen plasma induces photocurrent enhancement across the entire series, and recorded photocurrents show similar saturation levels. Large photocurrents are also recorded with 2 µm silicon membranes. LED pulses of 10 ms, ~4.3 W cm^{-2} and 532 nm are used (power, 19 mW; spot size, 0.75 mm). Boxes bind the IQR divided by the median; whiskers extend 1.5 ± IQR. All datapoints are plotted. Each box is calculated from at least three different locations on four separate samples for $N_{meas} \geq 12$. Experimental groups that are paired, such as photocurrents from the same sample, are measured before and after the oxygen plasma treatment. Statistics are calculated using Tukey's honestly significant difference test. *P* values for comparisons are shown: $^*P < 0.05$; $^{**}P < 0.001$; all non-significant (NS) comparisons had a *P* value > 0.8. Ctrl, control; norm., normalized. **d**, Representative photocurrent traces recorded from the stain-etched wafers.

In the absence of the standard p–i–n or p–n doping regime, the stain-etching-derived heterojunction was able to generate strong photocurrents upon light illumination. This fast and simple stain etching technique was performed under ambient temperature and pressure, using only wet etching solution, and without the need for any instrumentation. Notably, the oxygen plasma treatment that passivated the pore surface with a thin silicon oxide layer enabled a further 4-fold to 10-fold enhancement of the photocurrents. Electron dispersive X-ray spectroscopy confirmed oxidation of the silicon surface; the oxygen content after plasma treatment increased from 4.9% to 18.8% (Supplementary Fig. 6). Besides increasing the hydrophilicity of the material such that water and ions could access the nanoscale pores, we believe the oxygen plasma may have eliminated radiative surface recombinations[36], given that the characteristic

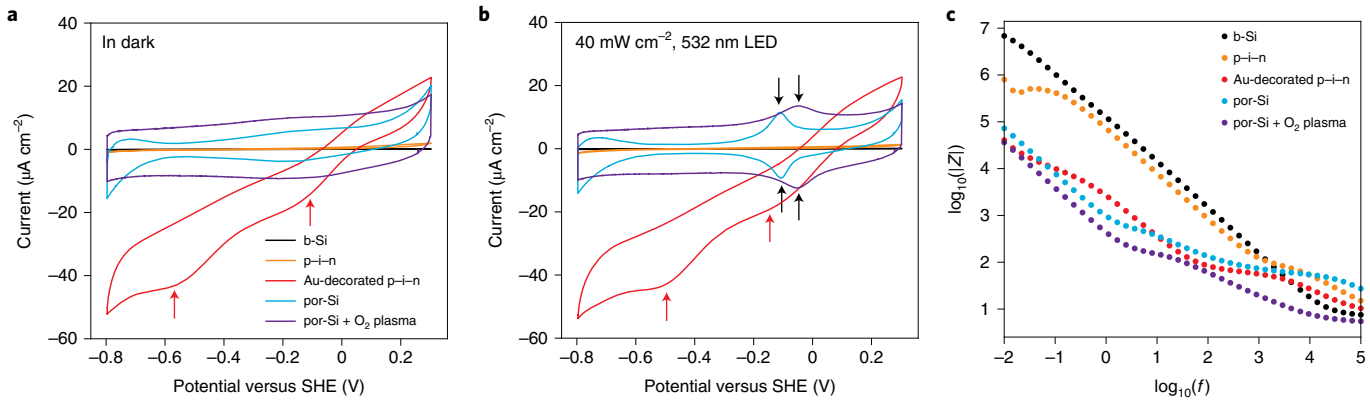

Fig. 4 | Electrochemical analysis of the nanoporous silicon. a, CV of silicon electrodes in the dark shows improved pseudocapacitive performance of the nanoporous silicon (por-Si) and oxygen plasma-activated silicon. The results are compared with those collected from bulk silicon (b-Si), p–i–n silicon and Au-decorated p–i–n silicon. Solution was 0.5 M K_2SO_4, pH 6.3. SHE, standard hydrogen electrode. **b**, Under light illumination, reversible-redox peaks are identifiable in nanoporous silicon, which may be attributed to an oxygen reduction reaction on the surface of the material. Black arrows indicate reversible-redox peaks in nanoporous silicon, and red arrows indicate irreversible redox peaks in a gold-decorated p–i–n junction. **c**, Electrochemical impedance spectroscopy of silicon electrodes shows that stain etching combined with oxygen plasma treatment reduces impedance (Z) in the entire range of frequencies (f). Two electrodes of each type were fabricated, and representative results are shown.

orange fluorescence was completely quenched upon plasma treatment (Supplementary Fig. 7).

The fabrication approach is also compatible with the processing of ultrathin, soft and flexible silicon membranes (thickness, ~2 μm) fabricated from silicon-on-insulator substrates. For silicon membranes, prolonged etching times over 40 s caused the breakdown of the heterojunction (Supplementary Fig. 8). But if the supportive crystalline silicon layer was not completely etched (due to the vertical progression of the etching front), the heterojunction generated photocurrents sufficient for biomodulation experiments.

We studied how varying concentrations of nitric acid in the etching solution affected heterojunction generation, and found that 1% nitric acid concentration was optimal for a 10 s stain etching time (Supplementary Fig. 9). Additionally, we investigated iron(III) ion and vanadium(V) oxide as alternative oxidants for stain etching, but their performance was lower than that of nitric acid (Supplementary Fig. 10). We attribute this lower performance to the suboptimal pore morphology, which had a more solid structure than the spongy surface created by nitric acid (Supplementary Fig. 11). Notably, we found that stain etching of n-type and intrinsic silicon wafers did not result in the creation of photoelectrochemical materials (Supplementary Fig. 12). We attribute this behaviour to the dopant-dependent energy levels produced in the silicon substrate upon porosification (Supplementary Fig. 13). These results support our proposed porosity-based heterojunction mechanism (Fig. 1a). Finally, we added surfactants in the etchant solution to avoid gas bubble accumulation and micropillar formation upon etching. Results showed dramatically reduced photoelectrochemical currents (Supplementary Fig. 14), suggesting that gas bubble templating (Fig. 2c) may be critical in forming the light-trapping structures.

Electrochemical and photoelectrochemical characterization

To understand the effects of stain etching and oxygen plasma treatment on the electrochemistry of the silicon, we performed standard electrochemical tests using wired electrodes. Figure 4a shows cyclic voltammetry (CV) curves of silicon electrodes with different surfaces (such as bulk silicon, stain-etched p-type silicon and p–i–n silicon with or without gold decoration). Stain etching improved the capacitance of the electrode interface over the flat wafer, and oxygen plasma treatment resulted in further enhancement. Additionally, when performing scans with 532 nm light irradiation (Fig. 4b), a pair of reversible-redox peaks were observed, which may be attributed to an oxygen reduction reaction on the porous surface[37]. This photoelectrochemical process is suggested by hydrogen peroxide production as detected through the dye degradation assay (Supplementary Fig. 15). This electrochemical behaviour is functionally different from that of our previously reported gold-decorated p–i–n junction[5], which showed strong but irreversible redox peaks (marked on the CV curve in Fig. 4a,b). Furthermore, electrochemical impedance spectroscopy (EIS) showed that the combination of stain etching and oxygen plasma reduced the impedance of the electrode over the entire range of frequencies (Fig. 4c). Impedance reduction may be attributed to the increase in surface area available for current injection and increased hydrophilicity of the surface, which reduces the barrier for ion transfer to and from the solution. Electrical impedance spectra can be described using Randles equivalent circuit with a restricted diffusion element to account for ion transfer through the nanoporous material (Supplementary Fig. 16).

We studied the stability of the silicon heterojunction in phosphate buffered saline (PBS) under illumination. We found no degradation in photocurrent between samples that underwent pulsed illumination of 14,000 pulses and samples stored in the dark for the same time period (Supplementary Fig. 17). This observation is in sharp contrast to our previously reported gold-decorated p–i–n junction[5], where a degradation of 30% in generated photocurrent was observed after only 1,000 pulses. The improved device performance supports our CV findings that the photoelectrochemical processes occurring on the nanoporous silicon surface may be more reversible, as opposed to the irreversible redox reaction on the gold-decorated p–i–n junction. Although the nanoporous layer is prone to dissolution in PBS when stored for more than 48 h (Supplementary Fig. 17), chemical surface modification or deposition of passivation layers can further improve its stability, similar to the stabilization of photovoltaic cells[38]. We found that atomic layer deposition can improve the material stability and increase the lifespan of the photoelectrochemical effects (Supplementary Fig. 17).

We investigated the dependence of the photoelectrochemical currents on the power and wavelength of the illumination light. While the materials generated large photoelectrochemical currents under visible and NIR light (Supplementary Fig. 18), ultraviolet (UV) light illumination did not elicit a photoresponse. We attribute this absence of photoresponse to the increased scattering

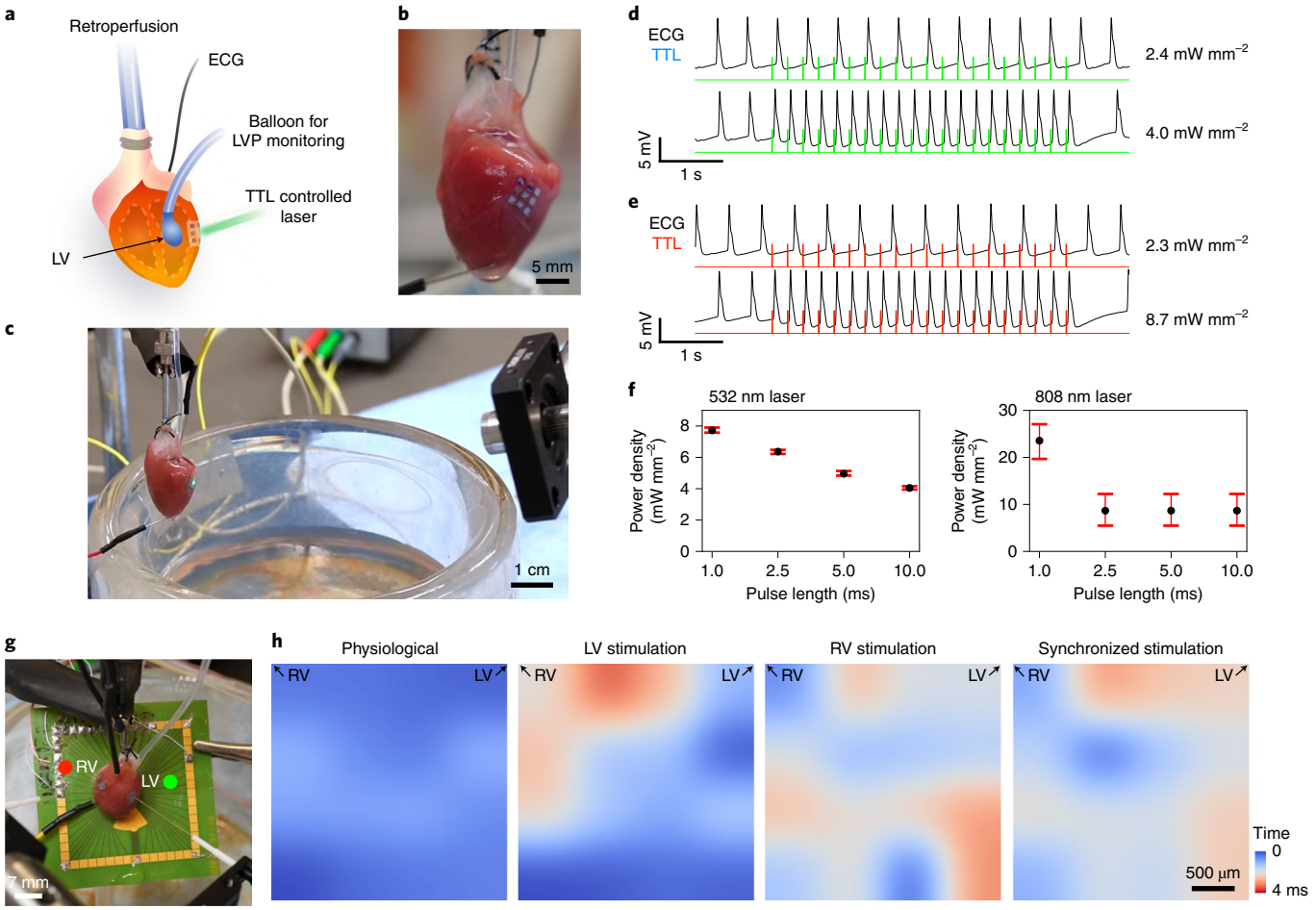

Fig. 5 | Pacing of isolated hearts ex vivo. a, Schematic of experimental set-up used for isolated heart in the Langendorff apparatus. LVP, left ventricular pressure. **b**, Photograph of the membrane attached to the heart on the left ventricular wall. **c**, Photograph of 532 nm laser illuminating the membrane attached to the isolated heart. **d**, Synchronized ECG and transistor–transistor logic (TTL) signals showing heart stimulation at 4 Hz using a 532 nm laser with subthreshold (2.4 mW mm^{-2}) and supra-threshold (4.0 mW mm^{-2}) optical power densities. Subthreshold stimulation results in only small artefacts in the ECG trace; supra-threshold illumination demonstrates overdrive pacing. **e**, When the heart is stimulated using 808 nm lasers at 4 Hz, the threshold is higher, as 8.7 mW mm^{-2} is needed to achieve overdrive pacing. Results in **d** and **e** are representative of over four independent experiments performed with different membranes and hearts. **f**, Optical power threshold for stimulation of heart tissue with 532 and 808 nm lasers. The central point represents the lowest power setting for which uninterrupted pacing was observed. Error bars represent half of the distance to the nearest laser power setting to estimate power read-out limitations. **g**, Photography of fibre set-up and microelectrode array used in the dual chamber pacing experiments. A 532 nm laser (4 mW mm^{-2}) was used to stimulate the LV and an 808 nm laser (60 mW mm^{-2}) was used to stimulate the RV. **h**, Isochrone maps of the electrical propagation in the ex vivo heart show different patterns of electrical propagation for spontaneous, single chamber (LV or RV) or dual chamber optical pacing.

and absorption of UV wavelengths in the nanoporous layer, such that the UV photons cannot reach the buried heterojunction (~1 µm below the surface) and generate photocarriers. This observation highlights the dominant role of the nanoporous/non-porous heterojunction (that UV photons cannot reach) over that of the nanoporous/saline junction (that UV photons can reach) in producing the observed photoelectrochemical effect. Moreover, although NIR light, which is more attractive for clinical biomodulation applications, was found less effective, it is important to note that the entire stain etching protocol was optimized for 530 nm green light illumination. Thus, it is reasonable to expect that a protocol optimized for 808 nm light will yield a better photoresponse for this wavelength. To connect the optical properties of the material with photoelectrochemical performance, we performed microspectrometry of the silicon membranes before and after processing (Supplementary Fig. 19). We found that stain etching and oxygen plasma treatment increased transmittance of the silicon membrane, due to removal of part of the material, but reduced reflectance of the membrane. The overall light absorption of the membrane was only slightly increased after complete processing. Given that the recorded photocurrent level is improved by orders of magnitude upon stain etching, we believe that the charge-separating diode-like heterojunction (Fig. 1a), as opposed to the nanoporous antireflective layer, is responsible for the enhanced photoelectrochemical properties.

Ex vivo cardiac modulation

To demonstrate the utility of our free-standing device in converting low optical power into bioelectrical stimulation, we interfaced the device with isolated cardiac tissue in a Langendorff apparatus (Fig. 5a). Figure 5b shows an image of the device conforming to the soft curvilinear cardiac surface and interfacing with the left ventricle (LV). Capillary forces between the flexible membrane and the heart were enough to hold the device in place without any adhesives or physical modifications, despite the wet surface and buffer perfusion. An electrocardiogram (ECG) recording of the electrical activity of the heart showed a slow atrioventricular node rhythm (due to

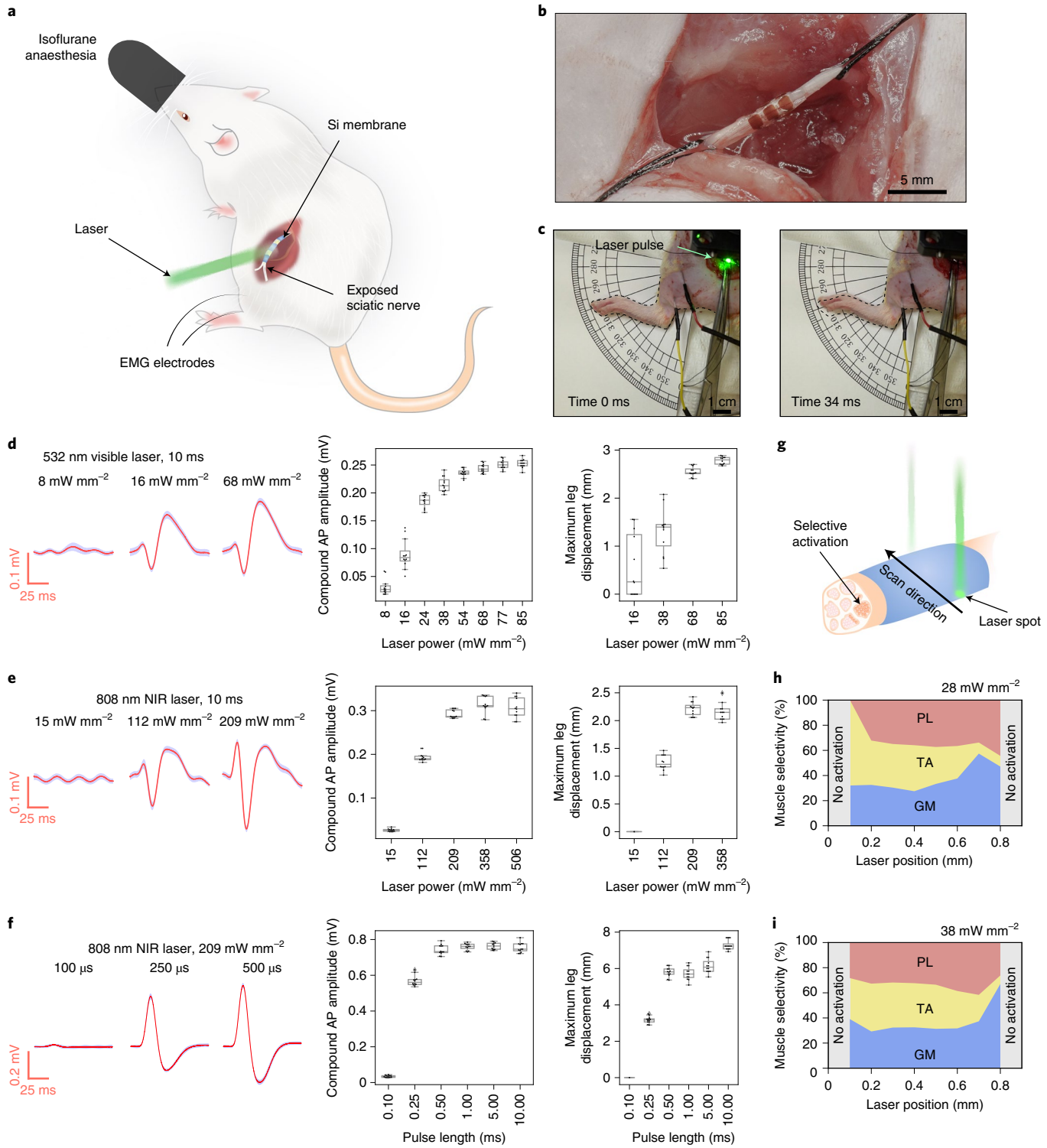

Fig. 6 | In vivo sciatic nerve stimulation. a, Schematic diagram of sciatic nerve stimulation in an acute in vivo rat model. **b**, Photograph of silicon membrane wrapped around the sciatic nerve. **c**, Still images from the video before (left) and after (right) photo-stimulation showing limb movement. **d**, Analysis of nerve stimulation with 10 ms visible 532 nm laser pulses. **e**, Analysis of nerve stimulation with 10 ms NIR laser pulses. **f**, Analysis of nerve stimulation with different NIR laser pulse lengths. Functional analysis of nerve stimulation in **d**–**f** is achieved through analysis of the EMG signal (left), maximum amplitude of the compound AP (centre) and maximum leg displacement distance (right) for the same 12 subsequent stimulation events at a frequency of 1 Hz. EMG signals at selected conditions are presented as an average; shaded area encompasses ± s.d. For compound AP amplitude and maximum leg displacement, the boxes bind IQR divided by the median, and whiskers extend 1.5 ± IQR. All datapoints are plotted, unless not detected. Data in panels **d** and **e** were recorded in the same experimental set-up with only a change of the applied laser, and data in panel **f** were acquired in a separate experiment. All results are representative of at least four independent experiments using different membranes and rats. **g**, Schematic diagram of a laser scanning and selective nerve activation. **h**,**i**, Selectivity index for a muscle stimulation with different laser positions and power. GM, gastrocnemius medialis; TA, tibialis anterior; PL, plantar interossei.

removal of the atriums). Upon application of light pulses (Fig. 5c), the heart immediately synchronized to the frequency of the light pulses (Fig. 5d, Supplementary Videos 1 and 2 and Supplementary Fig. 20) due to the effective depolarization of the myocardium through injected photoelectrochemical currents. To determine the optical density required for overdrive pacing, we stimulated a heart with 532 nm and 808 nm lasers, as shown in Fig. 5d,e, respectively. We found that 532 nm light had a lower stimulation threshold than 808 nm light (Fig. 5f). We achieved an improved stimulation efficiency over previously reported nanowire-based materials[39]; as little as 4 mW mm^{-2} of light (532 nm) was sufficient to stimulate the heart compared to the previously used power of 3.5 kW mm^{-2} (ref. [39]). The radiant exposure (532 nm) is now on the same order of magnitude as that required for heart stimulation using optogenetics (0.3–2 mJ cm^{-2})[40]. A notable quality of our device is the ability to utilize NIR wavelengths (808 nm) for optical biomodulation that can penetrate into deep tissues[41]. This is another meaningful advantage over optogenetics, in which opsins have a distinct light absorption band limited to visible light with low tissue penetration capabilities. Moreover, the radiant exposure necessary to stimulate the heart with NIR light (~2 mJ cm^{-2}) was also lower than that required for the unaided infrared stimulation of embryonic hearts (800 mJ cm^{-2})[15].

As our device is completely free-standing, it can be positioned at any location on the heart, free of lead-associated limitations. This suggests that the device can be used for simultaneous stimulation at multiple sites for cardiac resynchronization therapy, similar to previously reported work[19], but without the need for genetic modifications. To demonstrate the applicability of dual chamber pacing, we have performed experiments using two devices, one placed on the LV wall and the other on the right ventricular (RV) wall (Fig. 5g). Additionally, we used a microelectrode array to map the field potential propagation throughout the myocardium, and observed different propagation waves under varying stimulation conditions (Fig. 5h). Two separate contractions were observed only when a sufficient time delay between the two pulses was used (Supplementary Fig. 21), which also depends on which pulse is leading in the stimulation. We believe that this preliminary result shows potential for application of the device in heart stimulations from multiple positions, which increases its versatility and therapeutic potential.

In vivo sciatic nerve modulation

Finally, we demonstrated the utility of the device in neuroregenerative applications and studied acute in vivo sciatic nerve biomodulation in rats (Fig. 6a). Figure 6b shows that the flexible device can wrap around the exposed sciatic nerve without any apparent breakage and can adhere to it without need for glue or suture. Illuminating the device with pulsed light resulted in an action potential (AP) that propagated through the nerve and moved the associated lower limb (Fig. 6c and Supplementary Video 3). In contrast to heart stimulation, where we observed binary, sub- or supra-threshold pacing effects, the sciatic nerve showed an intensity-dependent effect. We investigated stimulation of the nerve using 532 and 808 nm lasers and measured the compound AP amplitude and maximal leg displacement. Figure 6d,e and Fig. 6f show a correlation between the optical power densities and the pulse duration to the compound AP amplitude and leg displacement, respectively.

In this context, it is important to realize that the sciatic nerve is a bundle of nerves[42]; consequently, the different nerves within the sciatic bundle may have different stimulation thresholds and/or different distances from the silicon membrane. Thus, the intensity dependence of the optical stimulation may be attributed to the ability of higher electrical intensity to stimulate nerves with higher thresholds and penetrate deeper into the bundle. We used multichannel electromyography (EMG) recording from gastrocnemius medialis, tibialis anterior and plantar interossei muscles to study the activation selectivity (Fig. 6g and Supplementary Fig. 22). By adjusting the power and position of the laser beam (Fig. 6h,i), we were able to activate different muscles to a varying extent. In clinical application, controlling the intensity and selectivity allows tuning the stimulation to yield a therapeutic output while minimizing pain and discomfort. Additionally, the selectivity reduces inverse recruitment of muscle groups, which delays the onset of muscle fatigue[43]. While silicon membranes are not as selective as multipolar cuff and intrafascicular implants[44,45], the improvement in membrane pattern design and application of beams with smaller diameters may further increase selectivity. Finally, we were able to stimulate the limb with a pulse as short as 500 µs for a NIR laser, which corresponds to a radiant exposure of 10 mJ cm^{-2}, an exposure that is energetically efficient and safe for most tissues.

While our experiments operate on the exposed nerve, the method is easily translatable to standard post-operative stimulation methods that employ implanted optical fibre cannulas (Supplementary Fig. 23 and Supplementary Video 4). Although in this proof of concept we used a glass fibre cannula, soft and flexible hydrogel-based optical fibres[46] can be used to deliver light to the interfacing nerve in vivo. Additionally, deep red- and NIR-induced photocurrent generation may enable fully remote transdermal stimulation using a NIR transmission window[41]. Moreover, the thin polydimethylsiloxane (PDMS) used here as a support layer for the silicon membrane can be avoided or replaced with hydrogel-based conduits to improve adhesion and retention of the electrode after wound closure.

Outlook

The approach we describe in this study combines fabrication simplicity with high functional efficiency. Thus, we believe that the porosity-based heterojunction is a promising candidate for future translational research on bioelectronic therapies. Our method enables fabrication without sophisticated instrumentation, allowing researchers to develop optoelectronic devices for biomedical applications cost efficiently. Moreover, the use of pristine p-type silicon, which is broadly regarded as biocompatible, for the main building block of the optoelectronic stimulation device is an advantage from a regulatory perspective, as an application of multi-material composites introduces additional safety concerns due to cross-talk between components. Although the instability of the material may pose some limitations, our preliminary surface modification experiments showed promising results that suggest that the stabilization of the materials can be easily tuned to meet the desired therapeutic timescale.

Online content

Any methods, additional references, Nature Research reporting summaries, source data, extended data, supplementary information, acknowledgements, peer review information; details of author contributions and competing interests; and statements of data and code availability are available at https://doi.org/10.1038/s41563-022-01249-7.

Received: 13 August 2021; Accepted: 6 April 2022;
Published online: 26 May 2022

References

1. Feiner, R. et al. Engineered hybrid cardiac patches with multifunctional electronics for online monitoring and regulation of tissue function. *Nat. Mater.* **15**, 679–685 (2016).
2. Fang, H. et al. Capacitively coupled arrays of multiplexed flexible silicon transistors for long-term cardiac electrophysiology. *Nat. Biomed. Eng.* **1**, 0038 (2017).
3. Xu, L. et al. 3D multifunctional integumentary membranes for spatiotemporal cardiac measurements and stimulation across the entire epicardium. *Nat. Commun.* **5**, 3329 (2014).
4. Kim, D. H. et al. Epidermal electronics. *Science* **333**, 838–843 (2011).
5. Jiang, Y. et al. Rational design of silicon structures for optically controlled multiscale biointerfaces. *Nat. Biomed. Eng.* **2**, 508–521 (2018).

6. Feiner, R. & Dvir, T. Tissue–electronics interfaces: from implantable devices to engineered tissues. *Nat. Rev. Mater.* **3**, 17076 (2017).
7. Murphy, J. J. Current practice and complications of temporary transvenous cardiac pacing. *Brit. Med. J.* **312**, 1134 (1996).
8. Austin, J. L., Preis, L. K., Crampton, R. S., Beller, G. A. & Martin, R. P. Analysis of pacemaker malfunction and complications of temporary pacing in the coronary care unit. *Am. J. Cardiol.* **49**, 301–306 (1982).
9. Betts, T. R. Regional survey of temporary transvenous pacing procedures and complications. *Postgrad. Med. J.* **79**, 463–465 (2003).
10. Nolewajka, A. J., Goddard, M. D. & Brown, T. C. Temporary transvenous pacing and femoral vein thrombosis. *Circulation* **62**, 646–650 (1980).
11. Rossillo, A. et al. Impact of coronary sinus lead position on biventricular pacing: mortality and echocardiographic evaluation during long-term follow-up. *J. Cardiovasc. Electrophysiol.* **15**, 1120–1125 (2004).
12. Peschar, M., de Swart, H., Michels, K. J., Reneman, R. S. & Prinzen, F. W. Left ventricular septal and apex pacing for optimal pump function in canine hearts. *J. Am. Coll. Cardiol.* **41**, 1218–1226 (2003).
13. Wells, J. et al. Optical stimulation of neural tissue in vivo. *Opt. Lett.* **30**, 504–506 (2005).
14. Wells, J., Konrad, P., Kao, C., Jansen, E. D. & Mahadevan-Jansen, A. Pulsed laser versus electrical energy for peripheral nerve stimulation. *J. Neurosci. Methods* **163**, 326–337 (2007).
15. Jenkins, M. W. et al. Optical pacing of the embryonic heart. *Nat. Photon.* **4**, 623–626 (2010).
16. Jenkins, M. W. et al. Optical pacing of the adult rabbit heart. *Biomed. Opt. Express* **4**, 1626–1635 (2013).
17. McCall, J. G. et al. Preparation and implementation of optofluidic neural probes for in vivo wireless pharmacology and optogenetics. *Nat. Protoc.* **12**, 219–237 (2017).
18. Montgomery, K. L. et al. Wirelessly powered, fully internal optogenetics for brain, spinal and peripheral circuits in mice. *Nat. Methods* **12**, 969–974 (2015).
19. Nussinovitch, U. & Gepstein, L. Optogenetics for in vivo cardiac pacing and resynchronization therapies. *Nat. Biotechnol.* **33**, 750–754 (2015).
20. Koo, J. et al. Wireless bioresorbable electronic system enables sustained nonpharmacological neuroregenerative therapy. *Nat. Med.* **24**, 1830–1836 (2018).
21. Choi, Y. S. et al. Fully implantable and bioresorbable cardiac pacemakers without leads or batteries. *Nat. Biotechnol.* **39**, 1228–1238 (2021).
22. Piech, D. K. et al. A wireless millimetre-scale implantable neural stimulator with ultrasonically powered bidirectional communication. *Nat. Biomed. Eng.* **4**, 207–222 (2020).
23. Jiang, Y. & Tian, B. Inorganic semiconductor biointerfaces. *Nat. Rev. Mater.* **3**, 473–490 (2018).
24. Rotenberg, M. Y. & Tian, B. Talking to cells: semiconductor nanomaterials at the cellular interface. *Adv. Biosyst.* **2**, 1700242 (2018).
25. Silvera Ejneby, M. et al. Chronic electrical stimulation of peripheral nerves via deep-red light transduced by an implanted organic photocapacitor. *Nat. Biomed. Eng.* https://doi.org/10.1038/s41551-021-00817-7 (2021).
26. Yan, F., Bao, X.-M. & Gao, T. Photovoltage spectra of silicon/porous silicon heterojunction. *Solid State Commun.* **91**, 341–343 (1994).
27. Palsule, C. et al. Electrical and optical characterization of crystalline silicon/porous silicon heterojunctions. *Sol. Energy Mater. Sol. Cells* **46**, 261–269 (1997).
28. Suntao, W., Yanhua, W. & Qihua, S. Measurement and analysis of the characteristic parameters for the porous silicon/silicon using photovoltage spectra. *Appl. Surf. Sci.* **158**, 268–274 (2000).
29. Fang, Y. et al. Micelle-enabled self-assembly of porous and monolithic carbon membranes for bioelectronic interfaces. *Nat. Nanotechnol.* **16**, 206–213 (2021).
30. Jiang, Y. et al. Heterogeneous silicon mesostructures for lipid-supported bioelectric interfaces. *Nat. Mater.* **15**, 1023–1030 (2016).
31. Kolasinski, K. W. in *Handbook of Porous Silicon* (ed. Canham, L.) Ch. 4 (Springer, 2018).
32. Yerokhov, V. Y. & Melnyk, I. I. Porous silicon in solar cell structures: a review of achievements and modern directions of further use. *Renew. Sustain. Energy Rev.* **3**, 291–322 (1999).
33. Alhmoud, H., Brodoceanu, D., Elnathan, R., Kraus, T. & Voelcker, N. H. A MACEing silicon: towards single-step etching of defined porous nanostructures for biomedicine. *Prog. Mater. Sci.* **116**, 100636 (2021).
34. Hopcroft, M. A., Nix, W. D. & Kenny, T. W. What is the Young's modulus of silicon? *J. Microelectromech. Syst.* **19**, 229–238 (2010).
35. Jiang, Y. et al. Nongenetic optical neuromodulation with silicon-based materials. *Nat. Protoc.* **14**, 1339–1376 (2019).
36. Glunz, S. W. & Feldmann, F. SiO_2 surface passivation layers – a key technology for silicon solar cells. *Sol. Energy Mater. Sol. Cells* **185**, 260–269 (2018).
37. Nosaka, Y. & Nosaka, A. Y. Generation and detection of reactive oxygen species in photocatalysis. *Chem. Rev.* **117**, 11302–11336 (2017).
38. Tampo, H., Kim, S., Nagai, T., Shibata, H. & Niki, S. Improving the open circuit voltage through surface oxygen plasma treatment and 11.7% efficient $Cu_2ZnSnSe_4$ solar cell. *ACS Appl. Mater. Interfaces* **11**, 13319–13325 (2019).
39. Parameswaran, R. et al. Optical stimulation of cardiac cells with a polymer-supported silicon nanowire matrix. *Proc. Natl Acad. Sci. USA* **116**, 413–421 (2019).
40. Bruegmann, T. et al. Optogenetic control of heart muscle in vitro and in vivo. *Nat. Methods* **7**, 897–900 (2010).
41. Jacques, S. L. Optical properties of biological tissues: a review. *Phys. Med. Biol.* **58**, R37–61 (2013).
42. Ushiki, T. & Ide, C. Three-dimensional organization of the collagen fibrils in the rat sciatic nerve as revealed by transmission- and scanning electron microscopy. *Cell Tissue Res.* **260**, 175–184 (1990).
43. Koutsou, A. D., Moreno, J. C., del Ama, A. J., Rocon, E. & Pons, J. L. Advances in selective activation of muscles for non-invasive motor neuroprostheses. *J. Neuroeng. Rehabilitation* **13**, 56 (2016).
44. Badia, J. et al. Comparative analysis of transverse intrafascicular multichannel, longitudinal intrafascicular and multipolar cuff electrodes for the selective stimulation of nerve fascicles. *J. Neural Eng.* **8**, 036023 (2011).
45. Strauss, I. et al. Q-PINE: a quick to implant peripheral intraneural electrode. *J. Neural Eng.* **17**, 066008 (2020).
46. Guo, J. et al. Highly stretchable, strain sensing hydrogel optical fibers. *Adv. Mater.* **28**, 10244–10249 (2016).

Methods

All animal procedures were approved by the Institutional Animal Care and Use Committee of the University of Chicago in protocol number 72378.

Stain etching of wafers and membranes. Silicon wafers (p-type, orientation (100), resistivity 0.001–0.005 ohm cm; n-type, orientation (100), resistivity 0.001–0.005 ohm cm; i-type, orientation (100), resistivity 10,000 ohm cm) were obtained from Nova Electronic Materials. The wafers were diced using the Disco DAD3240 dicing saw. Some $5\times5\,mm^2$ pieces were used in photocurrent evaluation experiments, and $10\times10\,mm^2$ pieces were used for fabrication of the electrodes used in the photoelectrochemical measurements and fluorescence measurements. Polytetrafluoroethylene tweezers were used for all sample manipulation, from the initial to final washing steps. Directly before etching, wafers were washed in an ultrasonic bath for 5 min in acetone (Histological grade, A16P-4, Fisher) followed by 5 min in isopropanol (Certified ACS Plus, A416P-4, Fisher) and then stored in deionized water (18.2 Mohm, MicroPure UV/UF, ThermoFisher). All stain etching experiments were performed in concentrated hydrofluoric acid (HF, TraceMetal grade, A513-500, Fisher). Concentrated nitric acid (HNO_3, TraceMetal grade, A509-P500, Fisher), iron(III) chloride hexahydrate ($FeCl_3$, ACS reagent, 97%, 236489-500G, Sigma-Aldrich) and vanadium(V) oxide (V_2O_5, 99.6+%, 206422500, Acros Organics) were used as porous-silicon-forming oxidizers. Sodium dodecyl sulfate (SDS, BioReagent, ≥98.5% (GC), L3771-25G, Sigma-Aldrich), Pluronic P123 (435465, 250 ml, Sigma-Aldrich) and Tween 20 (P2887, 100 ml, Sigma-Aldrich) were used as surfactant additives. Solutions and chemicals were used as received without additional processing, and all experiments were performed at room temperature (24–26 °C). Directly before etching, HNO_3 was mixed with HF in specified v/v ratios, or $FeCl_3$, V_2O_5 and surfactants were dissolved at specified concentrations and the solution was deoxygenated for 30 min by bubbling with argon. Each etching series (a set of samples using the same etchant composition and time) used approximately 10 ml of freshly prepared etchant and was performed in a fresh polypropylene dish. Silicon wafer samples were transferred from a water bath to the etching solution, moved along the bottom of the dish with the tweezers for the first 10 seconds and left undisturbed for the specified amount of time. After etching, samples were soaked twice for 1 min in separate deionized water baths to remove the HF, soaked once for 1 min in isopropyl alcohol and dried using compressed nitrogen. The $5\times5\,mm^2$ samples were mounted on reclaimed-grade silicon wafers using double-sided tape to ease further handling, and silicon membranes were transferred and attached to a PDMS substrate using fresh wet oxide silicon wafers. PDMS casting solution was prepared by mixing PDMS base (Sylgard 184, Dow), PDMS cure (Sylgard 184, Dow) and hexane (anhydrous, 95%, 296090, 1 l, Sigma-Aldrich) in a 10:1:10 (w/w/w) ratio. The solution was then degassed under vacuum, spin coated at 4,000 r.p.m. onto the poly(methyl methacrylate)-covered microscope slide and cured at 65 °C for 45 min. All samples were stored in a desiccator under vacuum for prolonged periods between experiments (>2 h). Supplementary Fig. 24 shows optical microscopy photographs demonstrating the formation of colourful stains on the surface of the wafers and silicon membranes. The porous bulk wafer appears mostly black under the reflected light, and the silicon membrane shows iridescent stains due to thin-film interference. The difference in optical appearance is due to different substrate thicknesses and not different etching conditions.

Silicon membrane fabrication. Silicon-on-insulator wafers (p++; device, 2 µm, 0.001–0.002 ohm cm; handle, 10–100 ohm cm; buried oxide, 1 µm) were obtained from Ultrasil (Hayward). The photomask was designed using AutoCAD software and is shown in Supplementary Fig. 25 (also available as DXF file in an online repository). Fabrication followed standard lithography procedures. A thick positive resist AZ40XT-11D (MicroChemicals) was used as a mask for reactive ion etching. Patterns were exposed using the Heidelberg MLA150 direct writer, and uncovered silicon-on-insulator was removed using SF_6/CHF_3 (20 sccm:50 sccm) reactive ion etching (inductively coupled plasma, 600 W; radiofrequency, 60 W) in a Plasma-Therm inductively coupled plasma fluoride etcher with an etching rate of about 600 nm min^{-1}. Photoresist was stripped using AZ NMP (MicroChemicals), and wafers were washed in an ultrasonic bath for 5 min in acetone followed by 5 min isopropyl alcohol and dried using compressed nitrogen. Samples were submerged in concentrated HF (analytical grade, 48% to 51% in water, 223335000, Acros Organics) for 4–8 h to remove buried oxide layers. The membranes, together with the handle wafer, were subsequently soaked twice for 1 min in separate deionized water baths to wash off the HF. The wafers were soaked in an isopropyl alcohol bath for 1 min and moved to an acetone bath to ease interactions between the membranes and handle wafer. Finally, the free-floating membranes were transferred to a fresh isopropyl alcohol bath using separate wet oxide silicon wafers and stored at 4 °C before further processing.

Oxygen plasma processing. Stain-etched silicon samples were treated with 800 W oxygen plasma at 50 sccm without radiofrequency bias for 10 min in a Plasma-Therm inductively coupled plasma fluoride etcher. Free samples of silicon wafers were directly attached to the carrier wafers using vacuum mounting oil, and mounted samples and silicon membranes were attached with their respective carrier substrates.

Photocurrent measurement. Photocurrent measurements generally followed previously described methods[35]. The patch-clamp set-up integrated with an upright microscope (Olympus, BX61WI) with a ×20/0.5 numerical aperture water-immersion objective was used for photocurrent measurements. Light pulses were delivered using episcopic illumination with a dichroic mirror (for 365 nm, 532 nm and 625 nm LEDs, FF660-Di02-25×36, Semrock) or Thorlabs protected silver mirrors (for 808 nm laser, PF10-03-P01, PFR10-P01). Applied light sources and their validation are described in a separate subsection. Clamp voltage and current were measured using silver chloride electrodes and amplified using an AxoPatch 200B amplifier (Molecular Devices). Voltage-clamp levels and light pulsing were digitally controlled using TTL or analogue signals delivered from a Digidata 1550 digitizer (Molecular Devices) controlled with Clampex software (Molecular Devices). Glass pipettes were pulled in a P-97 micropipette puller (Sutter Instrument), usually to a resistance of 1–4 MΩ and filled with ×1 PBS. In a typical measurement, the material was placed in a petri dish filled with ×1 PBS and positioned in the centre of the field of view. The pipette tip was lowered close to the surface of the material (<10 µm), and the measurement sequence was executed. The measurement sequence spans 400 ms, with a first voltage level of −0.5 mV between 100–300 ms. At 200 ms, a 10 ms light pulse was delivered to elicit a photoresponse from the material. The holding current was adjusted so that the current in the first voltage level was close to 0 pA (usually under 2,000 pA). Following the measurements, all samples were soaked in deionized water for 1 min, washed with deionized water, washed with isopropyl alcohol, dried using compressed nitrogen and stored under vacuum or immediately used for further experiments.

Photocurrent analysis. Photocurrents were analysed with a Python script working directly on the raw data files using the pyABF library. Total injected charge (Q_{tot}) was calculated through the integration of the area under the current transient during light illumination. Due to the high capacitive photocurrents in the material, the faradaic charge was calculated through fitting the last 20% of the current transient to the exponential decay equation: $I(t)=A\exp^{kt}+I_f$, where $I(t)$ is current, t is time, I_f is the faradaic current and A and k are constants. Poor quality fits were obtained if more of the transient was used for calculations due to the supercapacitive behaviour of the material in the early charging stages, which does not follow the exponential trend. A nonlinear solver using the Trust Region Reflective algorithm implemented in the Scipy Python package was used for fitting. The faradaic current is assumed to stay constant during the illumination and was used to calculate the faradaic charge $Q_f=I_f\Delta t$. Finally, the capacitive charge was calculated by subtracting the faradaic charge from the total injected charge $Q_c=Q_{tot}-Q_f$. All recorded values were normalized to a measurement performed with 1 MΩ pipettes according to Ohm's law. The detected photocurrents were exported into the delimited text files for further analysis and plotting. Raw data and analysis scripts are available in an online repository. Only measurements that failed due to technical reasons (such as a broken pipette or a light pulse not fired) were excluded from the analysis. An unsatisfactory photoresponse was not considered a valid reason for a datapoint rejection. Photothermal currents in the wafer and membrane samples were not detected (Supplementary Fig. 26), and therefore they are ignored in the general analysis. Additional validation of the photocurrent analytical methods is described in Supplementary Fig. 27.

Electrochemical tests. CV and EIS were performed using a potentiostat (SP-200, BioLogic) controlled with EC-Lab software. A platinum wire was used as the counter electrode, an Ag/AgCl electrode (saturated KCl) as the reference electrode and a silicon wafer as the working electrode. The potentials were corrected to the standard hydrogen electrode potential using silver chloride electrode potential $E_{AgCl(3.5\,M)}=-0.2037$ V (ref. [47]). Light was delivered from the bottom of the set-up using a 532 nm Thorlabs LED. Some 0.5 M K_2SO_4 (ReagentPlus, >99%, P0772-250G) was used as an electrolyte. A Pyrex glass dish was used as a cell container. Cell temperature was not controlled and was measured to be within 24–26 °C, which was unaffected by the LED illumination. EIS was performed in potentiostatic mode at the open circuit voltage with a sinusoidal voltage amplitude of 25 mV. CV was measured at 20 mV s^{-1}, and the second CV cycle was plotted. Schematic and pictures of the photoelectrochemistry measurement set-up are shown in Supplementary Fig. 28. EIS data were fitted to electrical circuit models using ZFit solver, included in the EC-Lab software (v.11.43) in the range of 1 Hz–10 kHz.

Scanning electron microscopy. Scanning electron microscopy was performed using a Merlin scope (Carl Zeiss). Samples were mounted on aluminium sample holders using copper tape. Cross-sections were prepared by scratching the back side of the wafer using a diamond scribe, breaking the sample in half and mounting on a 90° sample holder using copper tape. Energy-dispersive X-ray spectroscopy was performed on the same microscope using an Oxford Ultim Max 100 energy-dispersive X-ray spectroscopy system, and data were analysed using AZTEC software (Oxford Instruments). Raw images with attached metadata are available in an online repository.

Focused ion beam milling. Samples for STEM were prepared using the Tescan LYRA3 focused ion beam scanning electron microscopy system equipped with a gallium ion gun. The lamella was lifted in situ with a tungsten manipulator and

transferred to the post on the copper transmission electron microscopy half-circle grid. A platinum layer (~1 µm) was deposited onto the sample to protect its surface during milling to the thickness of ~200 nm. Scanning electron microscopy images of the lamella are shown in Supplementary Fig. 29.

STEM. STEM was carried out using a 200 kV aberration-corrected JEOL ARM200F with a cold field emission source, which gives a spatial resolution ~0.8 Å. The high-angle annular dark-field detector angle was set to 90–270 mrad to give *Z*-contrast images. Diffraction patterns were taken in transmission electron microscopy mode. Images were processed using ImageJ software. Raw images displaying all recording parameters are available in an online repository.

Atomic force microscopy. Atomic force microscopy was performed with a Bruker Dimension Icon microscope using a ScanAsyst probe in automated peak force tapping mode. Gwyddion software was used to remove scars from the scans, crop the scan area and plot the three-dimensional model of the material surface. Raw data are available in an online repository.

Indentation. Modulus and hardness measurements were carried out using a TI950 Triboindenter (Bruker-Hysitron) with a Berkovich tip at the Scanned Probe Imaging and Development facility at the Northwestern University Atomic and Nanoscale Characterization Experimental Center. The loading–holding–unloading cycles were used for the nanoindentation test. A standard quartz substrate was used to calibrate the system before measurement on silicon samples. Indentation results obtained were analysed based on the method suggested by Oliver and Pharr[48]. Raw data and calculation summaries are available in an online repository.

Ex vivo heart stimulation. Isolated heart preparation followed methods described previously[29]. In short, an adult rat (males, 300–400 g body weight) was heparinized and anaesthetized using open-drop exposure of isoflurane in a bell jar configuration. The heart was removed and placed in ice cold HBSS buffer, and the aorta was cannulated in preparation for use in a Langendorff set-up. Oxygenated HEPES-buffered Tyrode's solution was perfused through the cannulated aorta after passing through a heating coil and bubble trap (Radnoti). The heart was placed in a water-jacketed beaker (Fisher Scientific) to maintain a temperature of 37 °C. The perfusion pressure was maintained at 80–100 mmHg. The sinoatrial node along with the atria were removed to lower the atrioventricular node pace. The perfusion and left ventricular pressure were monitored using a BP-100 probe (iWorx) connected to the perfusion line and a water-filled balloon (Radnoti) inserted into the LV, respectively. For ECG recordings, needle electrodes were positioned on the left ventricular wall and aorta, grounded on the cannula and connected to a C-ISO-256 preamplifier (iWorx). All signals (perfusion, left ventricular pressure and ECG) were amplified using an IA-400D amplifier (iWorx) and interfaced with a computer using a Digidata 1550 digitizer with Clampex software (Molecular Devices). The silicon membrane was placed on the left ventricular wall and adhered stably to the heart. The lasers were pointed at the membranes, and stimulation and recording were controlled using the Digidata 1550 digitizer. When only light pulses or only membranes were used in the experiment, no stimulation was observed. The heart could be paced only when both membranes and light pulses were present (Supplementary Fig. 30). For dual chamber pacing experiments, hexagon-shaped membranes were placed on the left and right ventricular walls, and light was delivered from 532 nm and 808 nm lasers through 200 µm core glass fibre cannulas (CFMC22L20, Thorlabs) coupled to a 200 µm multimode fibre (M86L01 and M84L01, Thorlabs) using a ceramic mating sleeve. Electrical mapping was performed using a 4×4 microelectrode array (0.7 mm spacing between electrodes) and recorded using an Intantech RHD USB interface board and RHD 16-channel input recording headstage. The signals were recorded at 10 kS s^{-1} in the 0.1–100 Hz bandwidth. Isochrone maps of the electrical propagation were calculated using the Python scripts available in the online repository. A timestamp of peak positive signal deflection for each contraction was determined, and the average was calculated for multiple signals. Gaussian interpolation was used for map rendering to improve readability.

Acute sciatic nerve stimulation. The sciatic nerve surgery followed methods described previously[29]. In short, an adult rat (10–24 weeks, males and females) was deeply anaesthetized with isoflurane (3–4%). The fur was removed from the hindquarters using surgical clippers and hair removal cream. An incision across the midline was made in the skin, and the fascial plane was opened between the gluteus maximus and the anterior head of the biceps femoris, exposing the sciatic nerve. The nerve was extruded using sutures, and the silicon membrane was wrapped around the nerve. For EMG recordings, stainless steel needle electrodes in an ungrounded configuration were inserted into the soleus and connected to a C-ISO-256 preamplifier (iWorx). The EMG signal was amplified using an IA-400D amplifier (iWorx) and interfaced with a computer using a Digidata 1550 digitizer with Clampex software (Molecular Devices). The lasers were pointed at the membranes, and stimulation and recording were controlled using the Digidata 1550 digitizer. Note that the data in Fig. 6d,e were collected from the same experiment (by changing only the laser source), while the data in Fig. 6f were collected from a different experiment, which accounts for the difference in recorded amplitudes. For the analysis of leg displacement, a protractor was placed under the leg for a distance reference. Videos of limb movement were recorded using a Sony α6100 camera with a 30 mm macro lens (E 3.5/30, Sony) at 60 frames per second. The videos were cropped and sliced using Adobe Premiere Pro, exported as an image sequence and imported into ImageJ for processing. The image sequence was set as an eight-bit greyscale stack. A Gaussian filter with 4 pixel radius was applied to the entire stack, and the intensity of the first frame was subtracted. A binary threshold was used to isolate the displacement distance, and the maximum displacement was measured under the first nail. If no movement was detected, a value of 0 was assigned to the pulse. An Intantech RHD USB interface board and RHD 16-channel bipolar-input recording headstage were used for multichannel EMG recording. The signals were recorded at 10 kS s^{-1} in the 0.1–200 Hz bandwidth. Parts of the skin were removed to expose the muscles, and silver wires were inserted into gastrocnemius medialis, plantar interossei and tibialis anterior muscles following the anatomical cues. Ground electrode was placed under the skin on the upper right body side of the animal, opposite the recording side. A rectangular silicon membrane was placed on the exposed sciatic nerve and was illuminated from above using 532 nm laser light pulses with a spot size of 0.5 mm. The laser collimator was installed on the manual linear translational stage, and the nerve was scanned along the diameter at steps of 0.1 mm. Twelve light pulses were delivered at each position, and EMG signals were recorded. Analysis of the recording was performed using Python analysis scripts, available in an online repository. In short, for each laser pulse, the maximum positive deflection of the EMG signal was calculated. The selectivity index for each laser position was calculated as suggested in the literature[44] using the equation $SI_n = \frac{EMG_{n,norm}}{\sum_i EMG_{i,norm}}$, where SI_n is a selectivity index for a muscle n, $EMG_{n,norm}$ is a normalized maximum positive signal deflection for muscle n and $\sum_i EMG_{i,norm}$ is the sum of the normalized maximum positive deflections for all muscles included in the analysis. The signal from the plantar interossei muscle was background corrected using an iterative polynomial smoothing algorithm implemented in the pybaselines package to remove the large drift coming from the limb movement. No activation was defined where no signals were observed. For acute stimulation with a closed muscle, 532 nm laser pulses were delivered using 200 µm core glass fibre cannulas (CFMC22L20, Thorlabs) coupled to a 200 µm multimode fibre (M86L01, Thorlabs) using a ceramic mating sleeve. The muscle was closed using nylon sutures.

Animal subjects. CD/SD rats were originally obtained from Charles River and were housed and bred in the animal facility at the University of Chicago. The animal room was maintained at a humidity of 40–60% and a temperature of 18–23 °C under a 12-h-light/12-h-dark cycle. The animals were allowed free access to food and water.

Numerical data processing and statistics. The analysis of numerical data and plotting were performed with Python scripts using the NumPy, Matplotlib, SciPy and Seaborn libraries. Statistics were calculated using the statmodels library by applying Tukey's honestly significant difference multiple comparison test.

Reporting summary. Further information on research design is available in the Nature Research Reporting Summary linked to this article.

Data availability

All data supporting the results of this study are presented in the manuscript or the Supplementary Information. All raw data are available at https://osf.io/abyq2/.

Code availability

Custom code used in this study is available at https://osf.io/abyq2/.

References

47. Kahlert, H. in *Electroanalytical Methods* (eds Fritz Scholz et al.) Ch. 15 (Springer Berlin Heidelberg, 2010).
48. Oliver, W. C. & Pharr, G. M. An improved technique for determining hardness and elastic modulus using load and displacement sensing indentation experiments. *J. Mater. Res.* **7**, 1564–1583 (1992).

Acknowledgements

We thank K. Watters for scientific editing of the manuscript. This work was supported by the US Air Force Office of Scientific Research (FA9550-18-1-0503, FA9550-20-1-0387), the National Science Foundation (NSF DMR-2105321, NSF CBET-2128140, NSF MPS-2121044) and the US Army Research Office (W911NF-21-1-0090). A.P. acknowledges support from the Materials Research Science and Engineering Center-funded Graduate Research Fellowship (NSF DMR-2011854). This work made use of the Pritzker Nanofabrication Facility at the Pritzker School of Molecular Engineering at the University of Chicago, which receives support from the Soft and Hybrid Nanotechnology Experimental (SHyNE) Resource (NSF ECCS-2025633), a node of the National Science Foundation's National Nanotechnology Coordinated Infrastructure; the Scanning

Probe Imaging and Development facility of the Northwestern University Atomic and Nanoscale Characterization Experimental Center, which has received support from the SHyNE Resource (NSF ECCS-2025633); the International Institute for Nanotechnology; and Northwestern's MRSEC programme (NSF DMR-1720139). We acknowledge the MRSEC Shared User Facilities at the University of Chicago (NSF DMR-1420709) and the shared facilities at the University of Chicago Materials Research Science and Engineering Center, supported by the National Science Foundation under award number DMR-2011854. We acknowledge the support of J. Jureller with imaging and materials characterization. A.P. thanks G. Olack for assistance with STEM sample preparation using focused ion beam milling. We thank F. Shi for the help on the STEM imaging; this work made use of instruments in the Electron Microscopy Service (Research Resources Center, University of Illinois Chicago).

Author contributions

B.T. supervised the research. A.P. and B.T. conceived the nanoporous/non-porous heterojunction concept. M.Y.R. initiated the project, made the initial observations and performed preliminary experiments. A.P. performed the majority of the experiments and data collection. J.S., P.L., Y.L. and J.P. assisted with the material characterization. J.Y. assisted with the in vivo experiments. A.P. wrote the computer code for data analysis. A.P. and M.Y.R. prepared the manuscript with input from all other authors.

Competing interests

University of Chicago filed provisional patent applications for the synthesis of porous silicon materials and their applications to biomodulation. Inventors: B.T., A.P. and M.Y.R. All remaining authors declare no competing interests.

Additional information

Supplementary information The online version contains supplementary material available at https://doi.org/10.1038/s41563-022-01249-7.

Correspondence and requests for materials should be addressed to Bozhi Tian or Menahem Y. Rotenberg.

Peer review information *Nature Materials* thanks Silvestro Micera, Nicolas Voelcker and the other, anonymous, reviewer(s) for their contribution to the peer review of this work.

nature portfolio

Corresponding author(s): Menahem Y. Rotenberg, Bozhi Tian

Last updated by author(s): 2022-4-1

Reporting Summary

Nature Portfolio wishes to improve the reproducibility of the work that we publish. This form provides structure for consistency and transparency in reporting. For further information on Nature Portfolio policies, see our Editorial Policies and the Editorial Policy Checklist.

Statistics

For all statistical analyses, confirm that the following items are present in the figure legend, table legend, main text, or Methods section.

n/a	Confirmed	
☐	☒	The exact sample size (*n*) for each experimental group/condition, given as a discrete number and unit of measurement
☐	☒	A statement on whether measurements were taken from distinct samples or whether the same sample was measured repeatedly
☐	☒	The statistical test(s) used AND whether they are one- or two-sided *Only common tests should be described solely by name; describe more complex techniques in the Methods section.*
☒	☐	A description of all covariates tested
☐	☒	A description of any assumptions or corrections, such as tests of normality and adjustment for multiple comparisons
☐	☒	A full description of the statistical parameters including central tendency (e.g. means) or other basic estimates (e.g. regression coefficient) AND variation (e.g. standard deviation) or associated estimates of uncertainty (e.g. confidence intervals)
☐	☒	For null hypothesis testing, the test statistic (e.g. *F*, *t*, *r*) with confidence intervals, effect sizes, degrees of freedom and *P* value noted *Give P values as exact values whenever suitable.*
☒	☐	For Bayesian analysis, information on the choice of priors and Markov chain Monte Carlo settings
☒	☐	For hierarchical and complex designs, identification of the appropriate level for tests and full reporting of outcomes
☒	☐	Estimates of effect sizes (e.g. Cohen's *d*, Pearson's *r*), indicating how they were calculated

Our web collection on statistics for biologists contains articles on many of the points above.

Software and code

Policy information about availability of computer code

Data collection	No unique software was used to perform data collection and manufacturer software was generally used. Potentiostat (SP-200, BioLogic) was controlled using EC-Lab software (v. 1.33, BioLogic). DigiData 1550 digitizer was controlled using Clampex software (v. 10.4.0.36, Molecular Devices). Fergie spectrometer was controlled using LightField software (v. 6.1, Princeton Instruments). Intantech RHD USB interface board was controlled using RHX software (v. 3.0.4, Intantech). TriboScan was used for nanoindentation measurement and analysis (v. 10.2.0.2, Bruker).
Data analysis	Analysis of numerical data and plotting was performed with Python (v. 3.8.12) scripts using NumPy (v. 1.22.1), Matplotlib (v. 3.5.1), Scipy (v. 1.7.3), pybaselines (v. 0.8.0) and Seaborn (v. 0.11.2) libraries. ABF files were opened using pyABF (v. 2.3.5) library. Statistics were calculated using statmodels (0.13.1) library by applying Tukey's honestly significant difference (HSD) multiple comparison test. Representative analysis scripts are available in an online repository. Electron microscopy images were processed using ImageJ (Fiji, v. 2.0.0-rc-6). Atomic force microscopy images were processed using Gwyddion (v. 2.56). Nanoindentation calculation was performed using TriboScan (Bruker). Energy dispersive X-ray spectroscopy data was processed using AZtec (v. 5.0 SP1, Oxford Instruments). Adobe Premiere Pro (v.15.4.0) was used for cropping and slicing video recordings. Rat limb movement analysis was performed using ImageJ (Fiji, v. 2.0.0-rc-6). Photomasks were designed in AutoCAD 2021 (v. R.47.0.0).

For manuscripts utilizing custom algorithms or software that are central to the research but not yet described in published literature, software must be made available to editors and reviewers. We strongly encourage code deposition in a community repository (e.g. GitHub). See the Nature Portfolio guidelines for submitting code & software for further information.

Data

Policy information about availability of data

All manuscripts must include a data availability statement. This statement should provide the following information, where applicable:

- Accession codes, unique identifiers, or web links for publicly available datasets
- A description of any restrictions on data availability
- For clinical datasets or third party data, please ensure that the statement adheres to our policy

All data supporting the results of this study is presented in the manuscript or the supplementary materials. All raw data is available at https://osf.io/abyq2/?view_only=de2a81534b7e44b38e8e7d9f557be89d.

Field-specific reporting

Please select the one below that is the best fit for your research. If you are not sure, read the appropriate sections before making your selection.

☒ Life sciences ☐ Behavioural & social sciences ☐ Ecological, evolutionary & environmental sciences

For a reference copy of the document with all sections, see nature.com/documents/nr-reporting-summary-flat.pdf

Life sciences study design

All studies must disclose on these points even when the disclosure is negative.

Sample size	For material characterization, sample size of N = 4 and triplicate measurement was chosen to account for variability in material preparation and accuracy of measurement which relies on manual positioning of glass micropipette. Further increase of sample size does not increase the power of the analysis necessary for drawing the presented conclusions. Sample size for electrical stimulation experiments was not predefined. Samples size was determined based on the laboratory experience and was deemed to be sufficient to demonstrate and characterize representative effects of photoelectrochemical stimulation. In general, for electronic stimulation, the positive effect is observed for the successfully processed and transferred devices, and no effect is observed otherwise. Therefore increase in the sample size does not further increase the power of statistical analysis.
Data exclusions	Representative images of experiments are shown in a manuscript and SI. Similar results from experimental repeats are not shown.
Replication	Ex vivo heart stimulation results are representative of over four independent experiments performed with different membranes and hearts. (as stated in Figure 5 caption) In vivo sciatic nerve stimulation results are representative of over four independent experiments using different membranes and rats. (as stated in Figure 6 caption) All animal experimental replicates were successful when membranes were not damaged or lost during handling and positioning. For material characterization studies, all experiments were successfully replicated at least 2 times with an exception of focused ion beam cross section preparation and STEM imaging, which due to the expensive nature of an experiment was performed only once.
Randomization	No randomization was performed. Single effect type (electrical stimulation) was evaluated and no known co-variates exist for such experiment. The experimental subjects were drawn from homogeneous population of laboratory rats, and no significant variability in response to electrical stimulation is expected. In all subjects no stimulation was observed using light pulses when no materials were applied, and positive stimulation outcome was observed with the materials when the determined light above power threshold was applied.
Blinding	Entirety of material preparation and animal experiments were performed by the main author, therefore no additional staff was available to perform blinded investigations in animal experiments. Photocurrent analysis was performed using numerical methods, therefore experimenter blinding does not contribute bias to the analysis.

Reporting for specific materials, systems and methods

We require information from authors about some types of materials, experimental systems and methods used in many studies. Here, indicate whether each material, system or method listed is relevant to your study. If you are not sure if a list item applies to your research, read the appropriate section before selecting a response.

Materials & experimental systems

n/a	Involved in the study
☒	☐ Antibodies
☒	☐ Eukaryotic cell lines
☒	☐ Palaeontology and archaeology
☐	☒ Animals and other organisms
☒	☐ Human research participants
☒	☐ Clinical data
☒	☐ Dual use research of concern

Methods

n/a	Involved in the study
☒	☐ ChIP-seq
☒	☐ Flow cytometry
☒	☐ MRI-based neuroimaging

Animals and other organisms

Policy information about studies involving animals; ARRIVE guidelines recommended for reporting animal research

Laboratory animals	Adult (10-16 weeks) Sprague-Dawley rats (female and male) originally obtained from Charles River were housed and bred in the animal facility at the University of Chicago. The rats were used as heart donors for ex vivo isolated heart experiments and as subjects in in vivo sciatic nerve stimulation.
Wild animals	No wild animals were used in this study.
Field-collected samples	No field-collected samples were used in this study.
Ethics oversight	All animal procedures were approved by the Institutional Animal Care and Use Committee of the University of Chicago in the protocol number 72378.

Note that full information on the approval of the study protocol must also be provided in the manuscript.